


## RESEARCH ARTICLE OPEN ACCESS

# Polysulfides From Inverse Vulcanization Used in Electronic Tongues for Heavy Metal Sensing

Stella F. Valle<sup>1,2</sup>  | Andrey Coatrini Soares<sup>1</sup> | Mário Popolin Neto<sup>3</sup> | Caue Ribeiro<sup>2</sup> | Luiz Henrique Capparelli Mattoso<sup>2</sup> | Osvaldo N. Oliveira Jr<sup>1</sup> 

<sup>1</sup>University of São Paulo (USP), São Carlos Institute of Physics (IFSC), São Carlos, SP, Brazil | <sup>2</sup>Embrapa Instrumentation, São Carlos, SP, Brazil | <sup>3</sup>Federal Institute of São Paulo (IFSP), araraquara Campus, Araraquara, SP, Brazil

**Correspondence:** Osvaldo N. Oliveira Jr ([chu@ifsc.usp.br](mailto:chu@ifsc.usp.br))

**Received:** 10 April 2025 | **Revised:** 18 June 2025 | **Accepted:** 22 June 2025

**Funding:** This work was supported by Fundação de Amparo à Pesquisa do Estado de São Paulo (2023/08862-3, 2018/22214-6).

**Keywords:** capacitance | e-tongue | sensor | sulfur

## ABSTRACT

Polysulfides (PS) are versatile sulfur-rich polymers synthesized via the inverse vulcanization of elemental sulfur, a simple one-pot method that transforms an abundant, low-cost residue into a functional material. In this work, we employed different PS structures as sensing units in an electronic tongue (e-tongue) to detect the metal ions  $\text{Hg}^{2+}$ ,  $\text{Ag}^+$ , and  $\text{Fe}^{3+}$ . Detection was based on impedance spectroscopy, with capacitance data from three sensors processed using a multidimensional projection technique and machine learning. The e-tongue distinguished the three metal ions at various concentrations, down to 1 nM for  $\text{Hg}^{2+}$ , with a silhouette coefficient of 0.95. This high efficiency may be attributed to sulfur domains in PS acting as multiple active sites for metal sorption and binding. Using machine learning within the framework of multidimensional calibration space (MCS), the accuracy in distinguishing metal ion concentrations reached ~99%.

## 1 | Introduction

Heavy metal ions are highly toxic pollutants that are nonbiodegradable and accumulate in the environment, representing a serious threat to ecosystems and human health even at low levels [1–3]. Straightforward, fast, and sensitive methods are essential to identify such low concentrations. Since traditional analytical techniques (e.g., atomic absorption spectroscopy and inductively coupled plasma mass spectrometry) involve expensive equipment, long analysis times, specialized personnel, among other drawbacks, efforts have been made toward cost-effective alternative detection methods [4, 5]. In this context, sensors are an interesting alternative as they can be designed into portable or even wearable devices, allowing real-time detection of analytes [6–10]. Electronic tongues (E-tongues) are particularly appealing due to their global selectivity [11]. These systems consist of

a multicomponent sensor array with cross-sensitivity, based on the combination of nonspecific sensing units, offering significant advantages in the analysis of complex samples [12].

Many types of materials can be used in the sensing units of e-tongues. They include metal nanoparticles which impart a high performance but are disadvantageous owing to their cost, multistep preparation, and toxicity [13, 14]. Elemental sulfur (ES) is an alternative material with nontoxic nature, low cost, and high availability as an industrial residue [13–17]. Additionally, sulfur's metal binding tendency is appealing for heavy metal sensing [4, 14, 18]. However, ES processing into functional products has been limited due to the fragility of the resulting materials and its immiscibility with most solvents [15, 16]. The inverse vulcanization method overcame these issues, producing functional sulfur-based polymers (i.e., polysulfides) [19]. It is a

This is an open access article under the terms of the [Creative Commons Attribution](https://creativecommons.org/licenses/by/4.0/) License, which permits use, distribution and reproduction in any medium, provided the original work is properly cited.

© 2025 The Author(s). *Journal of Applied Polymer Science* published by Wiley Periodicals LLC.

simple and direct one-pot reaction with no solvent use and no by-product formation, thus a sustainable and economically viable process [19–22].

Polysulfide (PS) functionality and properties can be easily tailored by modifications in the chemical structure or in the morphology [23]. These polymers have been studied for their dynamic covalent bonding, polarizability, high refraction index, and redox activity [13, 15, 16], in applications that include cathodes in lithium batteries [19, 24–26], optical materials for IR [27–30], and adsorbents for heavy metals [31–36]. The latter demonstrates PS affinity with different metal ions, most notably  $\text{Hg}^{2+}$  and  $\text{Fe}^{3+}$  [1]. The use of PS for heavy metal sensing was suggested by Crockett et al. (2016) while observing a chromic response from PS with  $\text{Hg}^{2+}$  addition; however, the application as a sensor was not tested by the authors [32]. In Liao et al. (2021) Cu nanoparticles were immobilized in PS for electrochemical glucose sensing [37]. Despite indications that PS assisted in Cu activity, the polymer was not explored as the sole active material [37].

Herein, a polysulfide-based E-tongue was developed to detect heavy metals. We intended to explore PS as a functional and easily prepared sensing material that features multiple available active sites with high affinity toward metal ions. For that, we evaluated the performance in the simultaneous detection of  $\text{Hg}^{2+}$ ,  $\text{Ag}^+$ , and  $\text{Fe}^{3+}$ . Measurements were taken with impedance spectroscopy, which does not require electroactive materials or reference electrodes [11]. Data processing and calibration were conducted with multidimensional projection and machine learning techniques.

## 2 | Materials and Methods

### 2.1 | Materials

All chemicals were used as received unless otherwise stated. Elemental sulfur (Synth, Brazil), 1,3-diisopropenylbenzene (Oakwood Chemicals, USA) and oleylamine (Sigma-Aldrich,

USA) were used to synthesize the polysulfides. Tetrahydrofuran (THF, Dinâmica, Brazil) was used to solubilize the polymers. The following reagents were used to prepare the heavy metal solutions:  $\text{HgCl}_2$  and  $\text{FeCl}_3 \cdot 6\text{H}_2\text{O}$  (Sigma-Aldrich, USA),  $\text{AgNO}_3$  and  $\text{Cr}(\text{NO}_3)_3$  (Dinâmica, Brazil),  $\text{PbCl}_2$ ,  $\text{CuSO}_4 \cdot 5\text{H}_2\text{O}$  and  $\text{MgCl}_2 \cdot 6\text{H}_2\text{O}$  (Êxodo Científica, Brazil), and  $\text{ZnSO}_4 \cdot 7\text{H}_2\text{O}$  (Vetec, Brazil).

### 2.2 | Polysulfide Synthesis

Polysulfides were prepared by the inverse vulcanization of elemental sulfur (ES) [19, 38], using different dienes and varying sulfur ratios, as indicated in Figure 1 and Figure S1. Two polymers were synthesized with 1,3-diisopropenylbenzene (DIB) as the diene, either with 50 wt% or 70 wt% of ES (S50-DIB and S70-DIB, respectively), in order to compare the effect of different sulfur contents on the sensing performance. Another polymer was prepared with 50 wt% ES and a mixture of dienes, namely DIB (35 wt%) and oleylamine (OL, 15 wt%), referred to as S50-DIB/OL. The aim was to compare polysulfides with similar ES contents but distinct diene structures. The synthesis was carried out by adding ES to a glass vial and heating it in an oil bath under constant stirring with a magnetic bar (700 rpm). After reaching  $160^\circ\text{C}$  and initiating ES ring-opening polymerization (ROP), the dienes were added dropwise, keeping vigorous stirring to ensure proper homogenization of the reaction medium. The reaction was maintained at ca.  $165^\circ\text{C}$  until vitrification at 10 min, followed by cooling the materials to room temperature.

### 2.3 | Characterization

Elemental compositions were obtained with CHNS elemental analysis (FlashSmart, Thermo Scientific). Fourier transform infrared (FTIR) spectroscopy measurements were conducted in a spectrophotometer (VERTEX 70, Bruker) using the ATR method at the range of  $4000\text{--}400\text{ cm}^{-1}$ . Differential scanning calorimetry (DSC) was performed with Q100 equipment

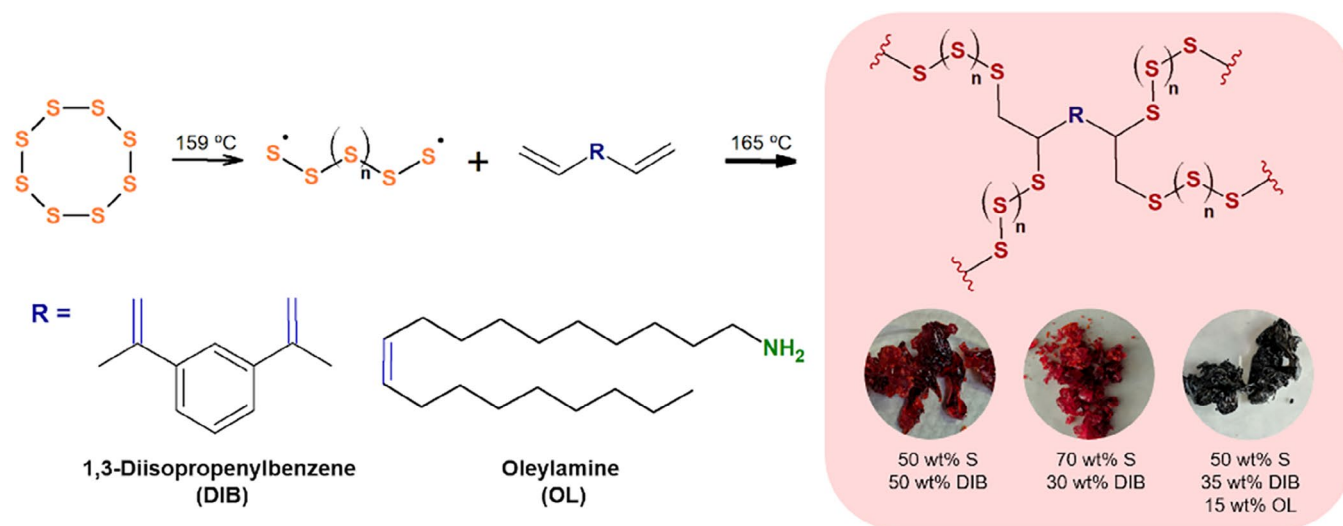


**FIGURE 1** | Chemical scheme of polysulfide formation by the inverse vulcanization of elemental sulfur with different dienes ( $R = \text{DIB, OL}$ ). [Color figure can be viewed at [wileyonlinelibrary.com](https://onlinelibrary.wiley.com)]

(TA Instrument) with temperatures ranging from  $-50^{\circ}\text{C}$  to  $200^{\circ}\text{C}$  at  $10^{\circ}\text{C}/\text{min}^{-1}$ , under nitrogen purge ( $50\text{ mL}\cdot\text{min}^{-1}$ ). Samples ( $3\text{--}8\text{ mg}$ ) were sealed in aluminum sample pans for the analysis. X-ray photoelectron spectroscopy (XPS) measurements were performed using a Scienta Omicron ESCA system equipped with a hemispherical analyzer (EAC-2000). A monochromatic Al K $\alpha$  source ( $h\nu = 1486.7\text{ eV}$ ) was used for excitation, and analyses were conducted under ultra-high vacuum. Spectral data processing was conducted with CasaXPS software using the C1s peak ( $284.8\text{ eV}$ ) as a reference for calibration. Scanning Electron Microscopy (SEM) images were acquired using a JSM-6510 (JEOL) microscope equipped with an energy-dispersive X-ray spectroscopy (EDS) detector. Prior to this, samples were placed on aluminum discs (stubs) with carbon tape, followed by coating with a thin carbon layer in an ionization chamber (Med 020, BALTEC). Polarization-modulated infrared reflection-absorption spectroscopy (PM-IRRAS) spectra were obtained with a KSV-PMI 550 spectrophotometer (KSV Instruments), using a spectral resolution of  $8\text{ cm}^{-1}$  and an incidence angle of  $81^{\circ}$ .

## 2.4 | Heavy Metal Detection Experiments

### 2.4.1 | Electrode Preparation

Gold interdigitated electrodes were manufactured by conventional photolithography, where  $6\times 6\text{ cm}$  BK7 glass slides were treated, firstly with hexamethyl-disiloxane (HMDS), followed by positive photoresist AZ4210 deposition by spin coating for 30 s. The slides were then cured on a metal plate at  $118^{\circ}\text{C}$  for 10 min and exposed to UV light for 10 s for polymerization of the photoresist from a lithographic mask for the interdigitated electrode. Then, the slides were treated with tetrabutylammonium hydroxide, followed by metallization via sputtering with chrome ( $100\text{ }\mu\text{m}$ ) and gold ( $20\text{ }\mu\text{m}$ ). The metalized slides were immersed in acetone to remove the metal deposited on the photoresist, generating electrodes with 50 pairs of interdigits  $10\text{ }\mu\text{m}$  wide,  $10\text{ }\mu\text{m}$  apart from each other. With this configuration, a capacitive profile was obtained. The electrode surface was modified by drop-casting  $4\text{ }\mu\text{L}$  of polysulfide solution ( $10\text{ mg}\cdot\text{mL}^{-1}$  in THF), followed by drying at room temperature for complete solvent removal. The electrodes went through a visual selection process to compose the electronic tongue.

### 2.4.2 | Electric Measurements and Data Acquisition

The PS-modified electrodes (S50-DIB, S50-DIB/OL, and S70-DIB) were then studied for discrimination of three heavy metal ions ( $\text{Hg}^{2+}$ ,  $\text{Ag}^{+}$ , and  $\text{Fe}^{3+}$ ) using electric impedance spectroscopy with an impedance analyzer Solartron 1260 A (Solartron Analytical, USA) (a setup scheme can be seen in Figure S2). The impedance data were acquired under an AC potential of  $50\text{ mV}$  in a frequency range from 1 to  $10^6\text{ Hz}$ , with 3 points per decade and measurements in triplicates. Capacitance data were obtained from the impedance values, calculated by the SMARt v3.3.1 software, and used in the following data processing steps. The electric measurements were conducted after exposing the sensing units to  $20\text{ }\mu\text{L}$  of different solutions, first with distilled water and then with  $10\text{ mM}$  solutions of either  $\text{Hg}^{2+}$ ,

$\text{Ag}^{+}$ , or  $\text{Fe}^{3+}$ . Then, solutions with different concentrations were measured separately for each metal ion, considering the safety limits recommended by regulatory authorities [3], namely  $0\text{--}50\text{ nM}$  for  $\text{Hg}^{2+}$ ,  $0\text{--}15\text{ }\mu\text{M}$  for  $\text{Ag}^{+}$ , and  $0\text{--}100\text{ }\mu\text{M}$  for  $\text{Fe}^{3+}$ . An experiment with potential interferents, that is, metal ions found in contaminated water samples ( $\text{Pb}^{2+}$ ,  $\text{Cu}^{2+}$ ,  $\text{Cr}^{3+}$ ,  $\text{Mg}^{2+}$ , and  $\text{Zn}^{+}$ ), was performed similarly. Another set of measurements was conducted with tap water samples collected in São Carlos (São Paulo, Brazil), at the geographical coordinate  $22^{\circ}00'44.8''\text{S}$   $47^{\circ}53'46.9''\text{W}$ . The tap water was spiked with either  $\text{Hg}^{2+}$ ,  $\text{Ag}^{+}$ , or  $\text{Fe}^{3+}$ , with a final concentration of  $10\text{ mM}$ . For this,  $50\text{ mM}$  stock solutions of each metal ion were previously prepared in distilled water.

### 2.4.3 | Data Processing With Multidimensional Projection Techniques

Information visualization and statistical treatment of the capacitance data were performed with Interactive Document Mapping (IDMAP) and Principal Component Analysis (PCA) techniques using PEx Software [39] to evaluate selectivity and the possible presence of false positives. In this technique, Euclidean distances are calculated between the capacitance spectra for different heavy metals samples in the original space  $X = \{x_1, x_2, x_3, \dots, x_n\}$  and projected onto a lower dimensional space, where  $Y = \{y_1, y_2, \dots, y_n\}$  is the mapping of  $X$  elements using Euclidean distances also in the new 2D space. The projections are calculated using Equation (1), where  $\delta_{\max}$  and  $\delta_{\min}$  are the maximum and minimum distances between data instances, respectively,  $(\delta(x_i, x_j))$  are Euclidean distances of samples in the original space and  $d(y_i - y_j)$  are the Euclidean distances in the lower dimensional space.

$$S_{IDMAP} \frac{\delta(x_i, x_j) - \delta_{\min}}{\delta_{\max} - \delta_{\min}} - d(y_i, y_j) \quad (1)$$

## 2.5 | E-Tongue Multidimensional Calibration

The three sensors array (e-tongue) under investigation comprises the architectures S50-DIB, S50-DIB/OL, and S70-DIB, providing each the capacitance value at 19 frequencies ( $1\text{--}10^6\text{ Hz}$ ), leading to 57 frequencies in total. For a robust analysis, the Multidimensional Calibration Space (MCS) method was used [40], supplying predictability and explainability (i.e., interpretability) for sensor calibration. MCS is based on classification models from machine learning [41, 42], which were used here to classify samples among four classes, namely Ag, Fe, Hg, and Interferent (samples of Pb, Cr, Cu, Zn, or Mg). MCS involves Decision Tree (DT) [41–43] models used to create calibrations, and ExMatrix [44] was used for interpretability. To assess DT's hyperparameters combinations and estimate performance, the Nested KFold Cross-Validation was conducted [45, 46]. While MCS supports model interpretability, the Nested KFold Cross-Validation delivers truthful performance estimation along with hyperparameters selection. In the Nested KFold Cross-Validation, two KFold Cross-Validation procedures are enclosed. Unlike with a single KFold Cross-Validation [42, 47], this strategy can avoid biased and optimistic (overestimation) performance metrics, which are typical issues with small datasets [45, 46]. The inner KFold Cross-Validation loop ( $k_{\text{inner}}$ ) performs for model selection, tuning the model hyperparameters

[42] such as tree depth, whereas model performance is carried out by the outer KFold Cross-Validation loop ( $k_{\text{outer}}$ ) [45, 46].

### 3 | Results and Discussion

#### 3.1 | Polysulfide Characterization

Polysulfides with different characteristics were obtained by the inverse vulcanization of ES (Figure 1). Both S50-DIB and S70-DIB formed red vitreous solids, the first showing more transparency while the latter was opaque owing to its larger sulfur content. S50-DIB/OL, on the other hand, formed a brittle glossy black material. The synthesis with only oleylamine as the diene (50wt%) was tested as well but it did not vitrify, remaining viscous and sticky. The addition of DIB proved advantageous, improving the material's workability. We produced polysulfides with different compositions and structures to compose an array of sensing units whose electrical responses to metal ions should differ. Since amino groups tend to bind to  $\text{Fe}^{3+}$  while sulfur has a strong affinity toward  $\text{Hg}^{2+}$ , we may be able to compare

**TABLE 1** | Mass ratios (wt%) of the reagents used to synthesize each polysulfide and elemental composition (wt%) of the obtained materials from CHNS analysis.

wt%	S50-DIB	S50-DIB/OL	S70-DIB
ES	50	50	70
DIB	50	35	30
OL	—	15	—
C	$43.4 \pm 0.8$	$44.0 \pm 0.3$	$26.4 \pm 0.5$
H	$3.6 \pm 0.1$	$4.4 \pm 0.1$	$2.0 \pm 0.1$
N	0	$0.9 \pm 0.0$	0
S	$57.3 \pm 3.7$	$62.9 \pm 0.3$	$83.7 \pm 3.3$

sensitivities and interrogate sensing mechanisms. The elemental composition of the materials was determined with CHNS analysis, as shown in Table 1. The polysulfides consist primarily of sulfur and carbon, although the sulfur contents exceeded the initial expectations. This could be explained by the partial volatilization of DIB molecules during the synthesis at elevated temperatures. In addition to sulfur and carbon, S50-DIB/OL contains a small amount of nitrogen, attributed to the oleylamine chains.

The FTIR spectra in Figure 2a confirm that polysulfides were effectively formed. Alkene vibration modes appear at  $3086\text{ cm}^{-1}$  and  $3007\text{ cm}^{-1}$  ( $\text{H}-\text{C}=\text{C}$  stretching) in DIB and OL spectra, respectively. These bands in PS spectra are either suppressed or reduced, indicating the reaction occurred successfully. The appearance of C-S stretching bands between  $630$  and  $600\text{ cm}^{-1}$  further confirms PS formation [48]. The absence of signals from  $2600$  to  $2550\text{ cm}^{-1}$  indicates that no S-H bonds were formed in parallel during the reaction. Moreover, intense S-S stretching bands are seen at  $467\text{ cm}^{-1}$  in all materials. Characteristic aromatic ring signals appear in all materials, including C-H stretching (at approximately  $3082$ ,  $3061$ , and  $3026\text{ cm}^{-1}$ ), C=C stretching (at  $1595$ ,  $1576$ , and  $1483\text{ cm}^{-1}$ ), C-H in-plane bending (at  $1121$ ,  $1103$ , and  $1082\text{ cm}^{-1}$ ), and C-H out-of-plane bending (at  $887$ ,  $793$ , and  $696\text{ cm}^{-1}$ ). Primary amine N-H bending occurs in the region between  $1707$  and  $1491\text{ cm}^{-1}$  in OL spectrum, while in S50-DIB/OL it appears as a broad weak band at  $1529\text{ cm}^{-1}$ . The complete band assignment is provided in Table S1 of the (SI). The thermal behavior of the materials was investigated with DSC (Figure 2b). The presence of unreacted ES particles within polysulfides is typically identified by ES melting transitions at  $109^\circ\text{C}$  (orthorhombic) and  $119^\circ\text{C}$  (monoclinic) [33, 49]. These peaks are absent or negligible in all the materials (see also Table S2), proving ES was fully consumed and formed stable bonds within the polymer structure. The DSC thermograms show the glass-transition temperatures ( $T_g$ ) at  $8.3^\circ\text{C}$ ,  $9.1^\circ\text{C}$ , and  $28.6^\circ\text{C}$  for S50-DIB/OL, S70-DIB, and S50-DIB, respectively. The significant increase of  $T_g$  in S50-DIB can be attributed to its

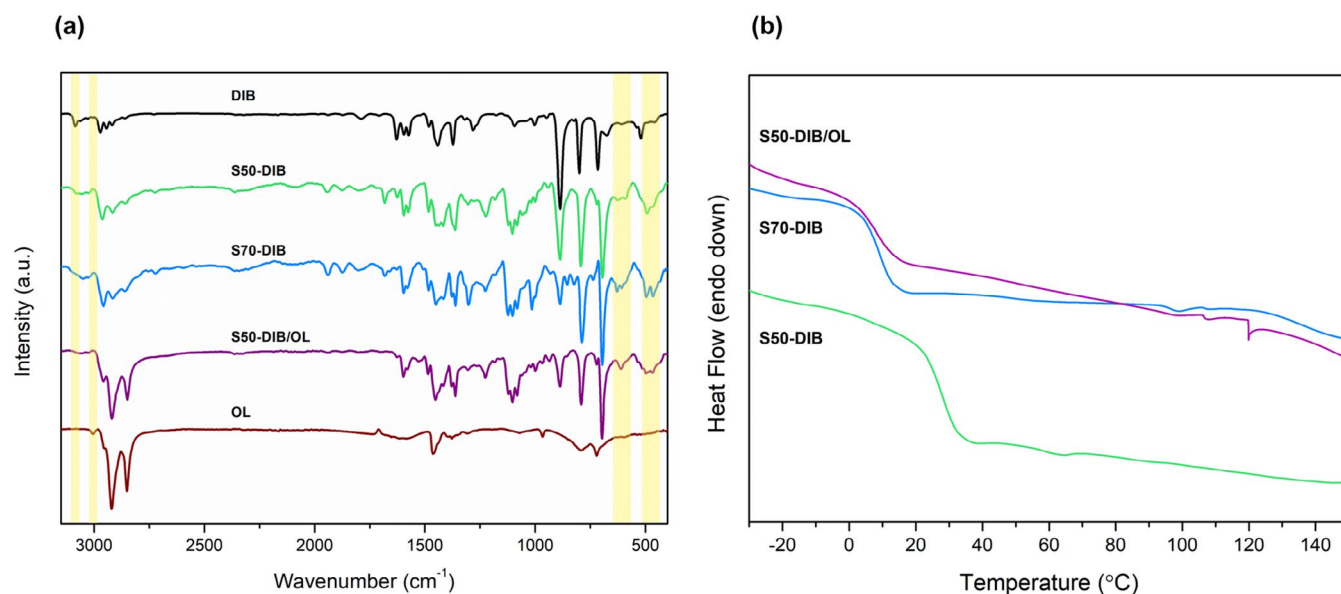


**FIGURE 2** | (a) FTIR spectra and (b) DSC thermograms of the polysulfide materials. [Color figure can be viewed at [wileyonlinelibrary.com](https://onlinelibrary.wiley.com/doi/10.1002/app.57382)]

higher DIB content, as aromatic rings tend to increase structure rigidity. In contrast, OL long chains promote more mobility to the polymeric structure, thus lowering the  $T_g$ .

### 3.2 | Detection of Heavy Metal Ions

The sensing units containing the polysulfides were used to detect  $Hg^{2+}$ ,  $Ag^+$ , and  $Fe^{3+}$  in aqueous solutions. These metals were selected based on their different electronic configurations and importance to environmental monitoring. Mercury ( $Hg^{2+}$ ) ions are among the most persistent and toxic metal ions. Even small exposures can cause problems like neurotoxicity, cardiovascular diseases, kidney and liver damage, and Minamata disease [1, 2, 50]. Silver is also hazardous to the environment and to humans, as it can easily bind to multiple metabolites causing cytotoxicity and organ failure [51, 52]. Despite being necessary for human metabolism, iron can be harmful if in excess, leading to hemochromatosis, dysfunction of organs, Parkinson's and Alzheimer's [2]. We were interested in investigating whether the different oxidation states of these hazardous metal ions could lead to distinct capacitance behaviors, as these differences are closely related to metal ligand preferences and could influence their interactions with sulfur in terms of affinity, number of coordination bonds, and stability. According to the hard/soft acid and base (HSAB) theory [53–55], for instance, soft Lewis acids like  $Hg^{2+}$  and  $Ag^+$  have a strong affinity with soft bases like sulfur, while hard acids (e.g.,  $Fe^{3+}$ ) tend to form weak interactions. Besides these aspects, the diverse ionic properties and electric conductivities of the ions could also play a role in the capacitance profile, especially in frequency regions where electrostatic interactions are prevalent.

The performance of the individual PS films as sensing units was evaluated as a preliminary test to compare their responses. The spectra obtained after exposure to pure water in Figure S4 show considerably higher capacitances for S70-DIB in the entire spectra. S50-DIB and S50-DIB/OL feature similar trends in mid-frequencies ( $10^2$ – $10^5$  Hz), while at lower frequencies ( $1$ – $10^2$  Hz) S50-DIB had slightly higher capacitance. Capacitance in mid-frequencies is predominantly related to the electrical properties of the coating material and its interface with the electrode, while at lower frequencies it depends on electrolyte–film interface interactions and the formation of an electrical double layer [56]. The similar behaviors of S50-DIB and S50-DIB/OL, in contrast to S70-DIB, indicate that the capacitive characteristics are mainly influenced by polymeric sulfur domains, which is consistent with the PS–sulfur role in batteries. Film thickness and morphology may also contribute to differences among the sensing units.

As anticipated, the electrical response varied across the different polysulfides, as shown in the capacitance spectra in Figure 3a–c, obtained after exposure to 10 mM of the three metal ions. The addition of silver ( $Ag^+$ ) significantly increased the capacitance in all films, likely due to its high electrical conductivity [57]. Migration of  $Ag^+$  ions within the polymer network and their interaction with sulfur may enhance the overall conductivity and capacitance of the polysulfides. In contrast, the presence of mercury ( $Hg^{2+}$ ) decreased the capacitance in all films. Although this effect on capacitance was modest, the impedance increased

significantly, especially for S50-DIB and S50-DIB/OL (Figure S5). This is possibly related to Hg binding to sulfur sites, reducing electron transfer and increasing charge transfer resistance. This effect was more pronounced in polysulfides with lower sulfur contents, which may become saturated more easily. Metal binding might also induce changes in the polymer chain conformation, altering the capacitance profile. For  $Fe^{3+}$ , the capacitance of S70-DIB was the most affected across all frequency regions. Contrary to expectations, the amino groups in S50-DIB/OL did not provide a conclusively specific response to iron [53–55]. The number of available ligands is crucial for an effective coordination arrangement with metal ions. The amino groups were probably sparsely distributed within the polysulfide structure due to the low content of N (Table 1) and random polymer configuration, thus hindering the coordination with  $Fe^{3+}$ .

The capacitance data were analyzed using the IDMAP multidimensional projection technique for each polysulfide film, with Euclidean distances employed to measure statistical differences between the detected metals. The silhouette coefficient was used as a metric to validate data clustering and analyte group separation, where values closer to 1 indicate better distinguishability of the samples, while S close to 0 and -1 indicate that distinction of the clusters is neutral and deleterious, respectively [58, 59]. The silhouette coefficients were calculated using Equation (2), where  $n$  is the number of samples,  $b_i$  is the minimum average Euclidean distances calculated between the  $i^{\text{th}}$  data point and data points of the other samples with different concentrations [59–61] and  $a_i$  is the average of the Euclidean distances between the  $i^{\text{th}}$  point and the data points of all the samples with the same concentration.

$$S = \frac{1}{n} \sum_{i=1}^n \frac{(b_i - a_i)}{\max(b_i, a_i)} \quad (2)$$

Figures 3d–f indicate that all polysulfide films could discriminate the capacitive responses for each metal ion and the distilled water control, with silhouette coefficients of 0.94 for S50-DIB and 0.97 for both S50-DIBOL and S70-DIB. The three sensing units were then combined in an e-tongue. The IDMAP plot in Figure 4a presents a clear separation of the sensing responses for the three metals, with a 0.97 silhouette coefficient. This should be expected as a good separation was already achieved with the individual sensing units. Using an e-tongue, nevertheless, is useful for the more challenging task of discriminating different concentrations of the heavy metals, particularly in ranges that are safe for human health. Regulatory authorities like the World Health Organization (WHO) and US Food and Drug Administration (FDA) recommend a limit in drinking water of  $0.001 \text{ mg/L}^{-1}$  for Hg ( $5 \text{ nM}$ ),  $0.1 \text{ mg/L}^{-1}$  for Ag ( $0.9 \mu\text{M}$ ), and  $0.3 \text{ mg/L}^{-1}$  for Fe ( $5.4 \mu\text{M}$ ) [1, 3, 62]. As shown in the IDMAP plots in Figure S6, the e-tongue could discriminate the various concentrations of each metal separately, with silhouette coefficients of 0.93, 0.95, and 0.96 for  $Hg^{2+}$ ,  $Fe^{3+}$ , and  $Ag^+$ , respectively. Figure 4b shows that the e-tongue can also distinguish multiple concentrations of the three metals simultaneously, providing a single IDMAP plot with a silhouette coefficient of 0.95. Note that the water cluster is distant from the analytes, and the data are grouped in separate regions of the IDMAP plot corresponding to each of the heavy metals, with no overlap of the concentrations. Moreover,

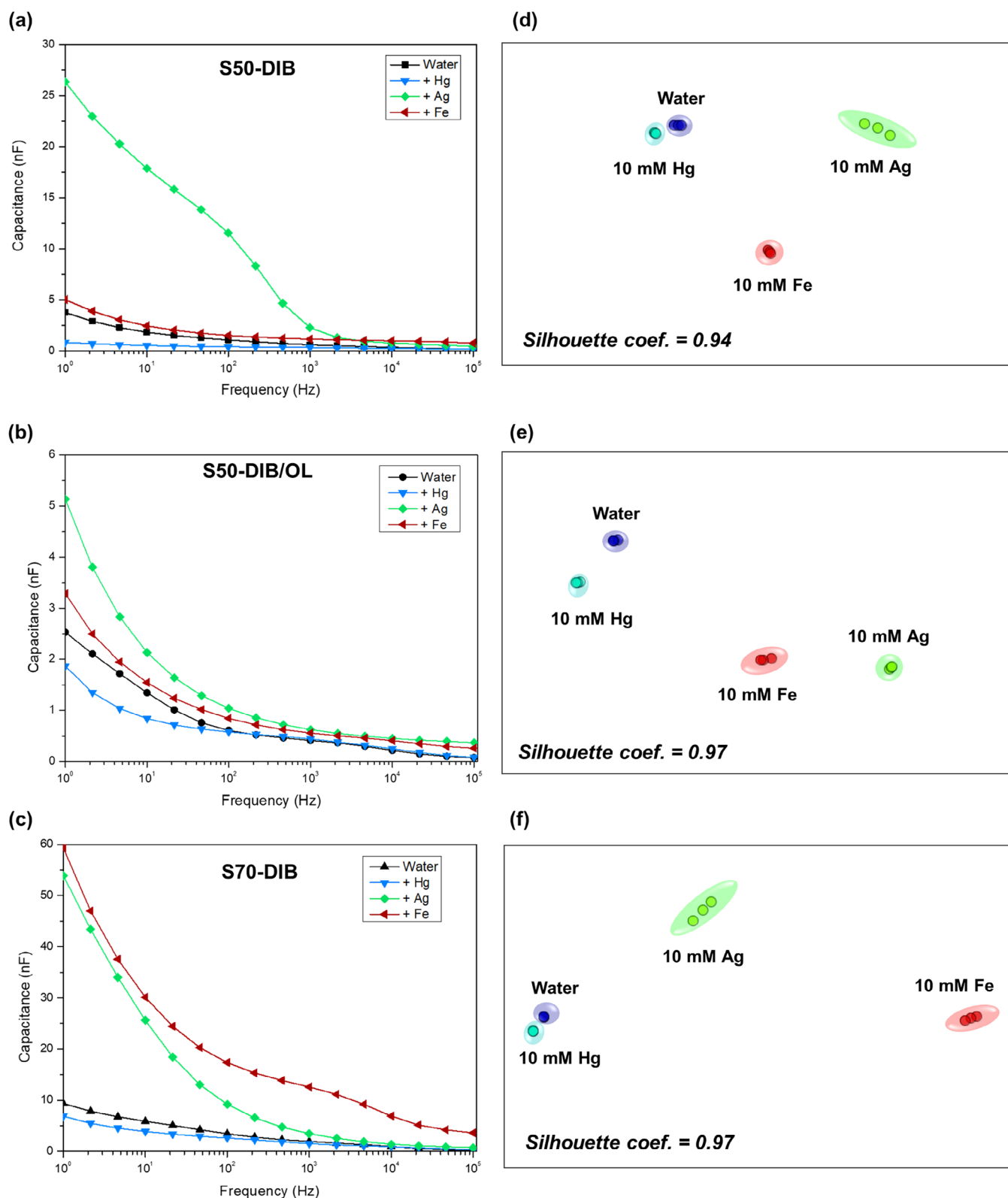


**FIGURE 3** | Capacitance spectra and IDMAP plots of S50-DIB (a, d), S50-DIB/OL (b, e), and S70-DIB (c, f) after exposure to pure water and 10 mM of  $\text{Hg}^{2+}$ ,  $\text{Ag}^+$ , and  $\text{Fe}^{3+}$ . [Color figure can be viewed at [wileyonlinelibrary.com](https://onlinelibrary.wiley.com)]

concentrations as low as 1 nM  $\text{Hg}^{2+}$ , 0.2  $\mu\text{M}$   $\text{Ag}^+$ , and 1  $\mu\text{M}$   $\text{Fe}^{3+}$  could be distinguished with the e-tongue. An experiment was also performed with interferent metal ions, viz.  $\text{Pb}^{2+}$ ,  $\text{Cu}^{2+}$ ,  $\text{Cr}^{3+}$ ,  $\text{Mg}^{2+}$ , and  $\text{Zn}^{2+}$  (Figure 4c), which are commonly found in environmental samples contaminated by mercury, silver, or iron.

We tested low concentrations within the recommended drinking water limits and a higher concentration (10 mM). Figure 4c shows that all metal ions remain well discriminated from each other, as well as from the target heavy metals, which indicates a potential applicability of this sensor array. The e-tongue was

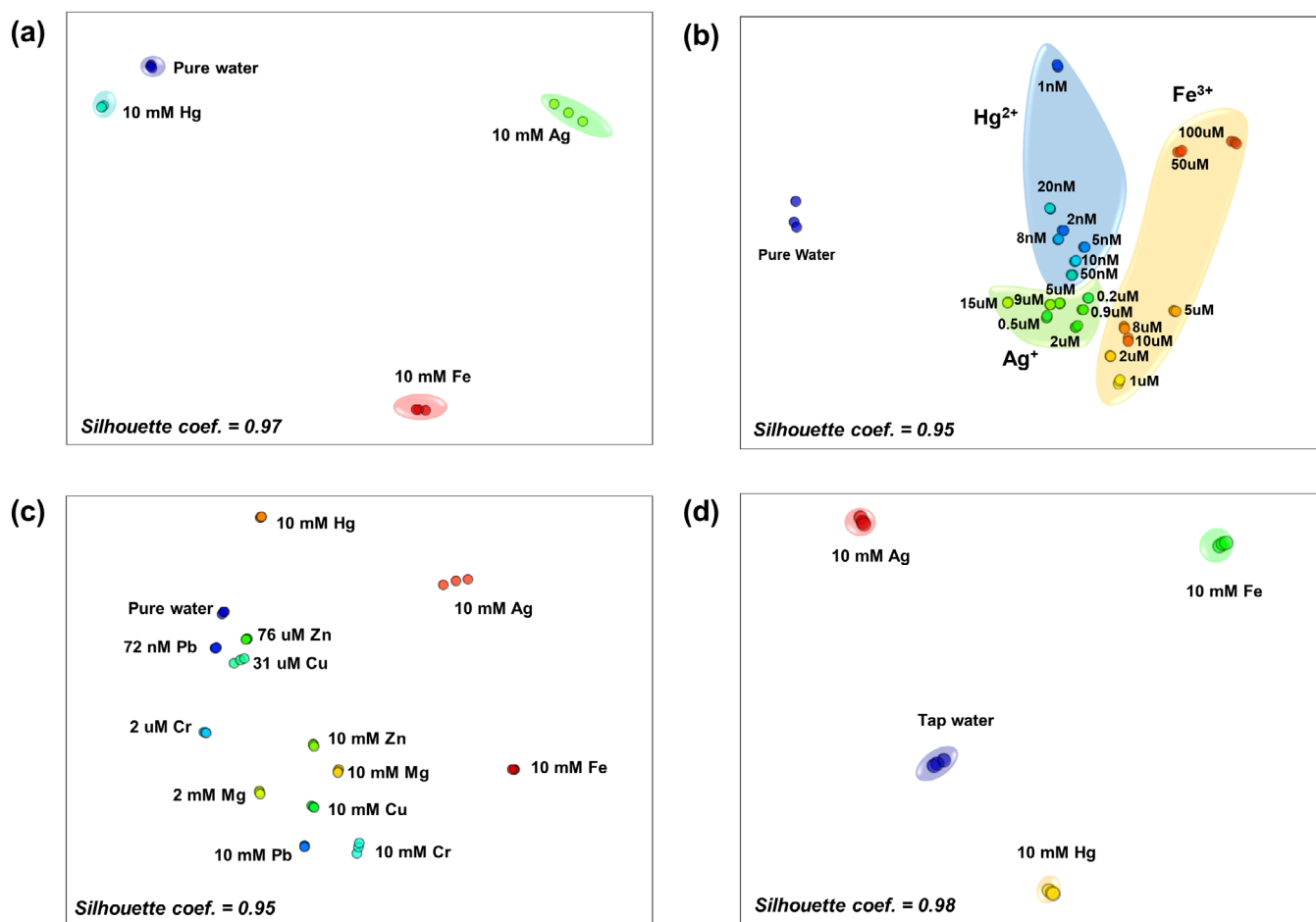


**FIGURE 4** | IDMAP plots of the e-tongue data: (a) for fixed concentrations (10 mM) and (b) multiple concentrations of Hg<sup>2+</sup>, Ag<sup>+</sup>, and Fe<sup>3+</sup>; (c) for different interferents (Pb<sup>2+</sup>, Cu<sup>2+</sup>, Cr<sup>3+</sup>, Mg<sup>2+</sup>, and Zn<sup>+</sup>); and (d) for tap water samples spiked with Hg<sup>2+</sup>, Ag<sup>+</sup>, and Fe<sup>3+</sup> (10 mM solutions). [Color figure can be viewed at [wileyonlinelibrary.com](https://onlinelibrary.wiley.com/doi/10.1002/app.57582)]

also evaluated for the discrimination of the targeted ions in a real-water sample, by spiking tap water with the metal ions. The e-tongue maintained a good performance, featuring a silhouette coefficient of 0.98 (Figure 4d), which demonstrates the robustness of the proposed platform against matrix effects and indicates its suitability for real-world application.

### 3.3 | Sensing Mechanism Investigation

Unveiling sensing mechanisms in liquid samples can be complex, as various factors may contribute to the detection process in impedance spectroscopy. Capacitance can be altered as a result of weak interactions of the sensing unit with the analyte, for instance, which may promote interfacial changes in the dielectric layer or even small variations on the film's surface [11]. Sensor response can also be related to metal binding, which may produce changes in the material's electrical properties or molecular conformation [63]. In order to investigate the nature of the interactions between the polysulfides and the heavy metals, we first verified whether the electrical response of the sensing units was reproducible after being exposed to samples of the metal ions and cleaned with distilled water. Figure S7 shows that while the response of the sensing units could be almost fully recovered after interacting with Ag<sup>+</sup> and Fe<sup>3+</sup>, the same did

not apply for Hg<sup>2+</sup>. The strong ionic character of Ag<sup>+</sup> and Fe<sup>3+</sup> probably favored electrostatic interactions instead of coordination interactions. In contrast, Hg<sup>2+</sup> ions were permanently adsorbed on PS owing to the strong binding tendency with sulfur domains. This strong interaction may be exploited when selectivity toward Hg is required. However, the Hg binding can also be a disadvantage to the reusability of the sensing units. There are, however, successful methods for PS recovery that could be explored in future studies, including treatments with acid solution and electrochemical stripping [35, 64].

A XPS analysis was performed to confirm whether Hg<sup>2+</sup> remains permanently adsorbed onto the PS structure. To identify this interaction and simulate the events at the electrode surface, S50-DIB powder was analyzed by XPS before and after exposure to Hg<sup>2+</sup> (methodology can be verified at SI). The recorded C1s and S2p regions of S50-DIB feature characteristic PS peaks (Figure 5a,b). The C1s spectrum in Figure 5a was deconvoluted into two peaks at binding energies (BE) of 284.7 eV and 285.9 eV, corresponding to C—C and C—S bonding, respectively [65, 66]. A  $\pi$ - $\pi^*$  satellite peak can also be seen at 290.1 eV (i.e., ~6 eV shift from the main peak), consistent with delocalized electrons from aromatic systems [67, 68]. The S2p region in Figure 5b shows two doublets from spin-orbit splitting of the S2p core level into S2p<sup>3/2</sup> and S2p<sup>1/2</sup> components (~1.2 eV separation and 2:1

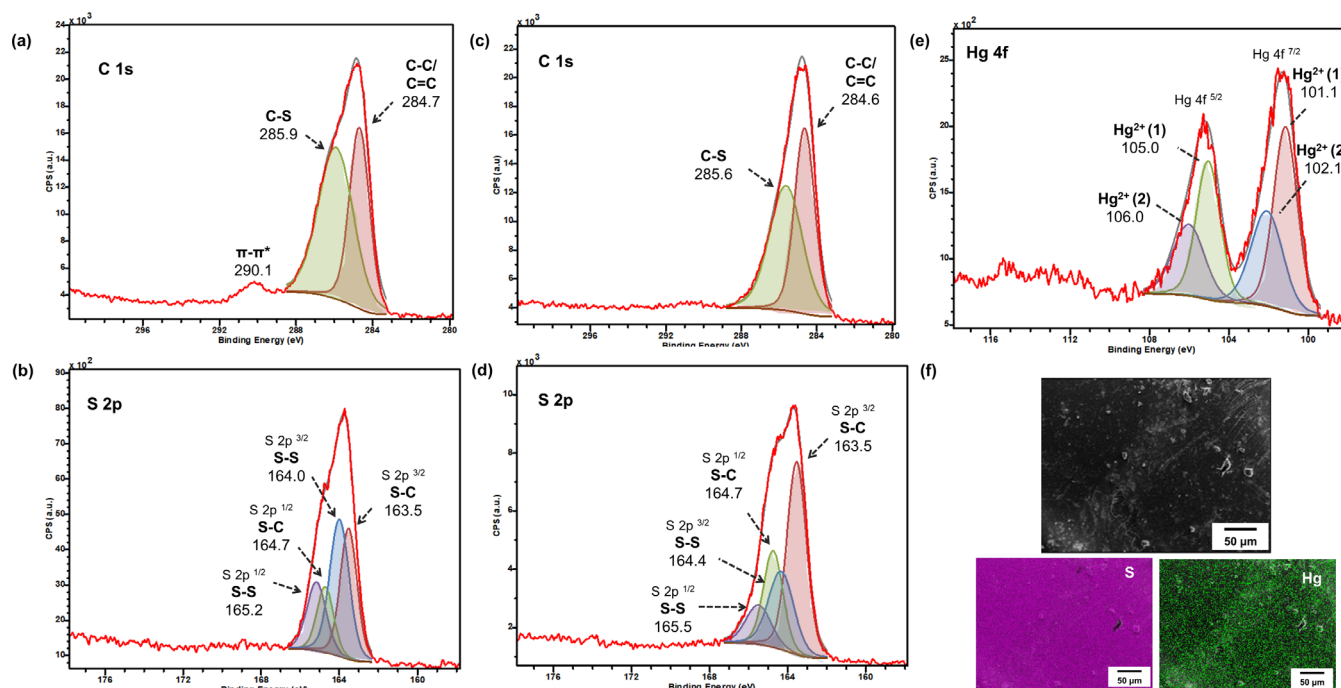


**FIGURE 5** | XPS spectra of S50-DIB polymer (a–b) before and (c–e) after Hg<sup>2+</sup> adsorption, with the corresponding (a, c) C1s, (b, d) S2p, and (e) Hg4f spectral lines. (f) SEM-EDS images of S50-DIB after Hg<sup>2+</sup> adsorption, with sulfur (pink) and mercury (green) mapping. [Color figure can be viewed at [wileyonlinelibrary.com](https://onlinelibrary.wiley.com/doi/10.1002/app.57582)]

intensity ratio) [66, 67]. These doublets appear at 163.5/164.7 eV and 164.0/165.2 eV, representing S-C and S-S bonds, respectively [66, 69, 70]. It is worth mentioning that, due to the random nature of the polymeric network, the PS material probably contains multiple overlapping S–C and S–S environments that lead to broader and less distinguishable doublets. No peaks were detected near 169 eV, indicating the absence of sulfates or oxidized sulfur species [66, 70].

After being exposed to Hg<sup>2+</sup>, S50-DIB exhibited subtle changes in the C1s and S2p spectra in Figure 5c,d, in addition to the appearance of Hg 4f peaks (Figure 5e), confirming Hg sorption by PS. C1s peaks slightly shifted to lower BE in Figure 5c, while the  $\pi-\pi^*$  satellite peak disappeared entirely, indicating a change in the overall electronic distribution induced by Hg interaction. In S2p spectra in Figure 5d, S-S peaks featured a more noticeable shift toward higher BE, suggesting a coordination interaction between S atoms and Hg. Additionally, S–S relative area reduction further supports sulfur participation in the sorption process. The Hg4f spectrum in Figure 5e features spin-orbit doublets (Hg4f<sup>7/2</sup> and Hg4f<sup>5/2</sup>,  $\sim 4.0$  eV splitting, 4:3 ratio) at 101.1/105.0 eV and 102.1/106.0 eV [71]. These are consistent with Hg<sup>2+</sup> sorption in distinct chemical environments, likely related to different S–S and S–C domains from the PS [72, 73]. Based on the absence of Hg<sup>0</sup> ( $\sim 99.8$  eV) and Hg<sup>1+</sup> ( $\sim 103.6$  eV) peaks, it can be concluded that Hg was adsorbed without being reduced or precipitating [73]. The XPS spectra survey from both samples can be seen in Figure S8. SEM-EDS elemental mapping was also performed, showing that while S50-DIB mainly contains sulfur and carbon (Figure S9), as evidenced in CHNS analysis (Table 1), mercury is homogeneously distributed over the PS surface after the polymer was exposed to the metal (Figure 5f), confirming the chemisorption.

A PM-IRRAS analysis was conducted to further investigate the sensing mechanisms of the films (Figure S10). Changes in film spectra after exposure to metal ions commonly indicate adsorption processes taking place, with changes in the dipole modes [74]. Overall, no significant modifications were identified in the studied range regarding molecular re-orientation (i.e., shift from parallel to perpendicular vibrations, and vice versa) [75]. This is possibly related to chain rigidity promoted by DIB groups. However, it is worth noting that the spectra range does not include IR lower frequencies ( $< 800$  cm<sup>−1</sup>) where C-S and S-S vibration modes are observed. The latter should be the most affected by interactions with the metal ions. Still, most of the spectra show a shifting or broadening of the bands. S50-DIB was the least affected, probably due to its greater DIB content. S50-DIB/OL displays wider bands with Hg and Ag, suggesting that the structure became less organized to accommodate these ions [75]. The same pattern can be observed in S70-DIB spectra in the presence of Ag and Fe. Both in the case of S50-DIB/OL and S70-DIB, PM-IRRAS modifications with specific metals are in line with capacitance changes to the same metals in Figure 3b,c.

### 3.4 | Using Machine Learning to Get a Multidimensional Calibration Space for the e-Tongue

Supervised machine learning methods currently achieve the highest performance in sensing applications where the data depend on multiple factors, as is often the case with e-tongues. In particular, the concept of a multidimensional calibration space (MCS) [40] can be used to provide a degree of interpretability when classifying different samples and enabling calibration in multiparameter analyses. Here, we constructed an MCS for the

e-tongue using Decision Trees (DT) represented in matrix form with the ExMatrix method [40, 44], as shown in Figure 6a. In this representation, logic rules appear as rows, features as columns, and rule predicates as cells. The cells define range values (rectangular shapes) of capacitance at specific frequencies (Hz), which are used to separate classes (i.e., Ag, Fe, Hg, and Interferents), visualized as categorical colors. The MCS for the e-tongue in Figure 6a consists of three dimensions (features/frequencies), selected from 57 frequencies available from the combination of sensor architectures (19 frequencies for each of the three sensors). Frequencies from two architectures, namely S50-DIB/OL and S70-DIB, were employed, yielding an average accuracy of 99% in predicting the metal ion.

The Nested KFold Cross-Validation procedure conveyed hyperparameters and performance estimation with  $k_{\text{outer}}=5$  and  $k_{\text{inner}}=5$  [45, 46]. The most important frequency was F215 Hz from S70-DIB (first column), with an importance value of 0.392. It is significant that only generic rules (high support) were generated—one for each class (i.e., Ag, Fe, Hg, and Interferents). Rules with the highest support (all rules from Figure 6a) are true (valid) for all samples from their class. Rule r4 (brown—first row) indicates that Interferent samples (Pb, Cr, Cu, Zn, or Mg) are characterized by higher capacitance values (rightmost rectangle) at F215 Hz in S70-DIB (first column) compared to Ag, Fe, and Hg. Rule r1 (olive—fourth row) reveals that Hg samples have lower capacitances (leftmost rectangle) at F21 Hz in S70-DIB (second column) than those of Ag and Fe. The latter ions are

distinguished by rules r3 (blue—second row) and r2 (orange—third row) using F21 Hz in S50-DIB/OL (third column), with Ag showing higher capacitance values (rightmost rectangle) than Fe. The frequency F21 Hz is relevant for both S50-DIB/OL and S70-DIB (second and third columns) architectures for distinguishing samples of Ag, Fe, and Hg (rules r3, r2, and r1—second to fourth rows).

MCS were also obtained for the individual sensing units, whose average accuracy is shown in Table 2. As expected, the accuracy is lower than for the e-tongue. The differences are not statistically significant given the standard deviations, but the interpretability in the MCS generated is not as simple, as indicated

**TABLE 2** | Average accuracy and standard deviation (SD) of the MCS calibrations, considering the 3 sensors array (e-tongue) and each polysulfide sensor individually. The calibrations concern prediction for samples among four classes: Ag, Fe, Hg, and Interferent (samples of Pb, Cr, Cu, Zn, or Mg).

Sensor	Accuracy (avg)	SD
Array (E-tongue)	0.9895	0.0211
S50-DIB	0.9684	0.0632
S50-DIB/OL	0.9573	0.0615
S70-DIB	0.9474	0.0577

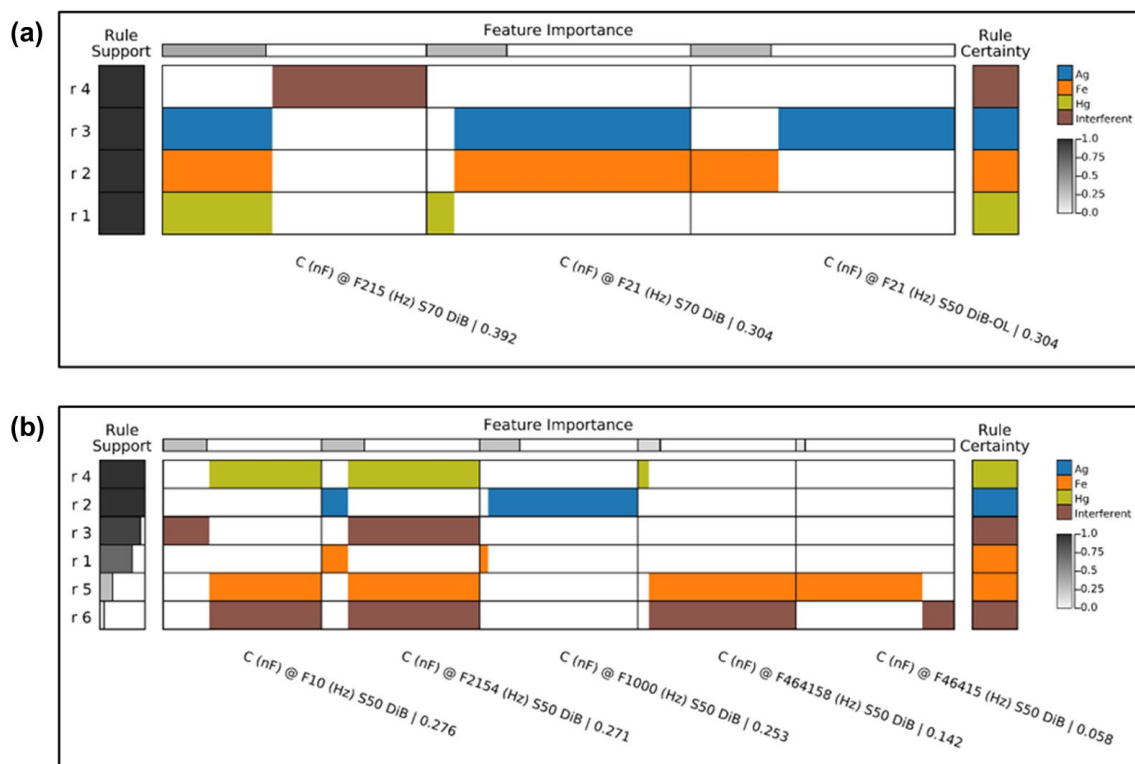


**FIGURE 6** | (a) MCS via DT model for the e-tongue. The MCS has 3 dimensions corresponding to 3 frequencies (features) selected among the 57 available (1 to  $10^6$  Hz from 3 sensors) Frequencies from 2 of 3 architectures are used, S50-DIB/OL and S70-DIB, from which F215 Hz in S70-DIB (first column) is the most important (value of 0.392). F21 Hz from both architectures are used (second and third column). (b) MCS via DT model for the S50-DIB architecture individually, with 5 dimensions which are 5 frequencies (features) selected among 19 available (1 to  $10^6$  Hz). Frequency F10 Hz (first column) is the most important (value of 0.276), and classes Fe (orange) and Interferent (brown) yield some complexity by not having a generic rule. [Color figure can be viewed at [wileyonlinelibrary.com](https://onlinelibrary.wiley.com/doi/10.1002/app.57582)]

**TABLE 3** | Comparison among impedimetric e-tongues for metal detection in literature. IS = impedance spectroscopy; VSA = anodic stripping voltammetry; FIA = flow injection analysis.

Detection method	Metal ions	Metric	Values	References
IS/VSA	K, Mg, Ca	Accuracy (%)	81.48 <sub>(IS)</sub> 91.60 (combined)	[79]
IS	Pb, Cu, Ni, Cd	Silhouette Coef.	0.98 (different metals with one concentration) 0.75 (different Pb concentrations)	[80]
IS	Hg, Al, Cu, Co	Silhouette Coef.	0.89	[81]
IS/FIA	Fe, Ba, Cd, Cu, Ni, Pb	PC1 + PC2 (%)	83	[82]
IS	Hg, Ag, Fe	Silhouette Coef.	0.95	This work
	Hg, Ag, Fe, Pb, Cu, Cr, Mg, Zn	Silhouette Coef.	0.95	
		Accuracy (%)	98.95%	

in Figure 6b for the S50-DIB sensing unit (the best performance taking sensing units individually). The latter MCS has 5 dimensions (features/frequencies) rather than 3 in the MCS for the e-tongue, and classes Fe and Interferent (orange and brown) require more than one single generic rule (rules r3, r1, r5 and r6—third to sixth row).

A straightforward comparison of the performances of e-tongues or other sensors in metal ion detection is a hard task owing to the diversity of metrics employed and the variety of experimental setups (e.g., targeted metals and concentrations tested). For heavy metal analysis, in particular, various studies are found using fluorescence [2, 18, 76] or electrochemical [77, 78] sensors/sensor arrays, but data on impedimetric e-tongues are less common. Nevertheless, it is possible to state that the accuracy of 99% achieved here by the PS e-tongue upon applying MCS is the highest in the literature, to the best of our knowledge. Table 3 features some of the works on metal ion detection with impedance spectroscopy, based on different sensing materials. The accuracy (~99%) presented here is higher than in the work of Lu et al. (2022) [79], for instance, while also encompassing a broader scope of metal ions and concentrations. Regarding silhouette coefficients, the PS-based e-tongue exhibited the best performance for simultaneous discrimination of metal ions with multiple concentrations [80–82].

In addition to outperforming other similar systems from the literature, some specific advantages of the proposed sensor array should be highlighted. In contrast to many sensing materials that require complex preparation, polysulfide synthesis is straightforward. Its production via inverse vulcanization aligns with green chemistry principles, offering high atom economy and a solvent-free process that eliminates the need for purification or additional steps. Primarily composed of elemental sulfur, PS is both cost-effective and less toxic than other conventional materials (e.g., metal oxides or nanoparticles). The high sulfur content also implicates in an intrinsic selectivity to detect heavy metals through specific interactions. Unlike other polymers used in sensing devices, PS functions as an active sensing material rather than just a passive substrate, while also

retaining the advantageous properties of polymers. Regarding the e-tongue operation, contrary to the more conventional electrochemical methods, for instance, impedance spectroscopy does not require electroactive materials or reference electrodes, which simplifies the operation and allows more flexibility in material selection [11]. E-tongue systems offer a key benefit regarding their ability to analyze complex mixtures rather than a single target, which is more suited to real-world samples. Moreover, e-tongue data processing involves multivariate analysis rather than a linear one-variable relation. In our sensor array, various points from the spectra were combined, so different types of interaction (e.g., electrostatic and metal coordination) collectively contributed to the analysis. This multifaceted sensing capability enhances both the sensitivity and selectivity of the platform.

## 4 | Conclusions

We have shown that polysulfides can be used successfully as active materials for heavy metal sensing, thus showcasing a new type of application for this class of polymers. A polysulfide-based e-tongue was fabricated and tested, combining impedance spectroscopy measurements from different sensing units with data processing through multidimensional projection techniques and multidimensional space calibration. The e-tongue was able to distinguish not only different heavy metal ions ( $\text{Hg}^{2+}$ ,  $\text{Ag}^+$  and  $\text{Fe}^{3+}$ ) but different concentrations of these ions simultaneously. The silhouette coefficient from IDMAP analysis was used as a validation metric, showing excellent results ( $>0.9$ ) for all of the combinations tested. Moreover, measurements with interferents ( $\text{Pb}^{2+}$ ,  $\text{Cu}^{2+}$ ,  $\text{Cr}^{3+}$ ,  $\text{Mg}^{2+}$ , and  $\text{Zn}^{2+}$ ) suggest that the e-tongue is capable of differentiating a wide scope of heavy metal ions. The MCS approach allowed the machine learning model to be interpretable. In addition to a high average accuracy of ~99%, the MCS of the e-tongue yielded only generic rules. In contrast, the MCS for a single sensor (S50-DIB) had a higher dimension and two support rules (not generic). Thus, combining the sensor units leads to a better performance in addition to a simpler, more generic calibration model. It was possible to determine

the frequency F21 Hz from both S50-DIB/OL and S70-DIB as an important contributor in distinguishing samples of Ag, Fe, and Hg. The frequencies and sensors used in these calibrations were selected by the DT model inference algorithm; however, it cannot be stated that alternative frequencies and sensor selections would not yield equivalent model performance. Overall, the present work offers new insights into the polysulfide role as a sensing material and provides a promising candidate for accurate and fast heavy metal sensing.

## Associated Content

Supporting Information. FTIR band assignments; Impedance spectra of the different PS films; IDMAP plot of each metal in varying concentrations; XPS survey spectra; PM-IRRAS spectra.

## Author Contributions

**Stella F. Valle:** conceptualization (lead), funding acquisition (equal), investigation (lead), methodology (equal), writing – original draft (lead). **Andrey Coatrini Soares:** conceptualization (equal), investigation (equal), methodology (equal), writing – review and editing (equal). **Mário Popolin Neto:** investigation (equal), methodology (equal), writing – original draft (equal). **Caue Ribeiro:** conceptualization (supporting), supervision (supporting), writing – review and editing (supporting). **Luiz Henrique Capparelli Mattoso:** conceptualization (supporting), supervision (supporting), writing – review and editing (supporting). **Oswaldo N. Oliveira Jr:** conceptualization (lead), data curation (lead), funding acquisition (lead), project administration (lead), supervision (lead), validation (lead), writing – original draft (lead).

## Acknowledgments

This work was supported by FAPESP (São Paulo State Research Foundation, #2023/08862-3, #2018/22214-6), CNPq (National Council for Scientific and Technological Development, #406925/2022-4), and FINESP (#01.24.0554.00). This study was also supported by the Brazilian Coordination for the Improvement of Higher Education Personnel (CAPES) - Finance Code 001. The authors thank the Group of Polymers “Prof. Bernhard Gross” (GP-IFSC/USP) and the National Nanotechnology Laboratory for Agribusiness (LNNA) for providing institutional support and facilities. The Article Processing Charge for the publication of this research was funded by the Coordenação de Aperfeiçoamento de Pessoal de Nível Superior - Brasil (CAPES) (ROR identifier: 00x0ma614).

## Data Availability Statement

The data that supports the findings of this study are available on request from the corresponding author.

## References

1. F. G. Müller, L. S. Lisboa, and J. M. Chalker, “Inverse Vulcanized Polymers for Sustainable Metal Remediation,” *Advanced Sustainable Systems* 7 (2023): 2300010.
2. P. Alam, N. L. C. Leung, J. Zhang, R. T. K. Kwok, J. W. Y. Lam, and B. Zhong, “AIE-Based Luminescence Probes for Metal Ion Detection,” *Coordination Chemistry Reviews* 429 (2021): 1.
3. S. Mukherjee, S. Bhattacharyya, K. Ghosh, et al., “Sensory Development for Heavy Metal Detection: A Review on Translation From Conventional Analysis to Field-Portable Sensor,” *Trends in Food Science and Technology* 109 (2021): 674–689.

4. G. Qiao, L. Liu, X. Hao, et al., “Signal Transduction From Small Particles: Sulfur Nanodots Featuring Mercury Sensing, Cell Entry Mechanism and In Vitro Tracking Performance,” *Chemical Engineering Journal* 382 (2020): 122907.
5. C. Liu, X. Chen, B. Zong, and S. Mao, “Recent Advances in Sensitive and Rapid Mercury Determination With Graphene-Based Sensors,” *Journal of Materials Chemistry A* 7 (2019): 6616–6630.
6. L. F. de Lima, A. d. S. M. de Freitas, A. L. Ferreira, C. C. Maciel, M. Ferreira, and W. R. de Araujo, “Enzymeless Glucose Sensor Based on Disposable Ecoflex®/Graphite Thermoplastic Composite Substrate Modified With Au@GQDs,” *Sensors and Actuators Reports* 4 (2022): 100102.
7. A. M. de Campos, R. R. Silva, M. L. Calegari, and P. A. Raymundo-Pereira, “Design and Fabrication of Flexible Copper Sensor Decorated With Bismuth Micro/Nanodendrites to Detect Lead and Cadmium in Noninvasive Samples of Sweat,” *Chem* 10 (2022): 446.
8. J. Heikenfeld, A. Jajack, J. Rogers, et al., “Wearable Sensors: Modalities, Challenges, and Prospects,” *Lab on a Chip* 18 (2018): 217–248.
9. Z. Bao, S. Lu, D. Zhang, G. Wang, X. Cui, and G. Liu, “Wearable Microneedle Patch for Colorimetric Detection of Multiple Signature Biomarkers In Vivo Toward Diabetic Diagnosis,” *Advanced Healthcare Materials* 13, no. 13 (2024): 2303511.
10. F. Han, T. Wang, G. Liu, et al., “Materials With Tunable Optical Properties for Wearable Epidermal Sensing in Health Monitoring,” *Advanced Materials* 34 (2022): 2109055.
11. A. Riul, C. A. R. Dantas, C. M. Miyazaki, and O. N. Oliveira, “Recent Advances in Electronic Tongues,” *Analyst* 135 (2010): 2481.
12. F. M. Shimizu, M. L. Braunger, and A. Riul, “Heavy Metal/Toxins Detection Using Electronic Tongues,” *Chem* 7, no. 1 (2019): 36.
13. R. Priyadarshi, A. Khan, P. Ezati, et al., “Sulfur Recycling Into Value-Added Materials: A Review,” *Environmental Chemistry Letters* 21 (2023): 1673–1699.
14. W. Lu, Z. Wei, W. Guo, et al., “Shaping Sulfur Precursors to Low Dimensional (0D, 1D and 2D) Sulfur Nanomaterials: Synthesis, Characterization, Mechanism, Functionalization, and Applications,” *Small* 19 (2023): 1095.
15. J. J. Griebel, R. S. Glass, K. Char, and J. Pyun, “Polymerizations With Elemental Sulfur: A Novel Route to High Sulfur Content Polymers for Sustainability, Energy and Defense,” *Progress in Polymer Science* 58 (2016): 90–125.
16. J. Lim, J. Pyun, and K. Char, “Recent Approaches for the Direct Use of Elemental Sulfur in the Synthesis and Processing of Advanced Materials,” *Angewandte Chemie International Edition* 54 (2015): 3249–3258.
17. D. A. Boyd, “Sulfur and Its Role in Modern Materials Science,” *Angewandte Chemie International Edition* 55 (2016): 15486–15502.
18. Z. Sun, H. H. Xing, M. Qing, et al., “From the Perspective of High-Throughput Recognition: Sulfur Quantum Dots-Based Multi-Channel Sensing Platform for Metal Ions Detection,” *Chemical Engineering Journal* 452 (2023): 139594.
19. W. J. Chung, J. J. Griebel, E. T. Kim, et al., “The Use of Elemental Sulfur as an Alternative Feedstock for Polymeric Materials,” *Nature Chemistry* 5 (2013): 518–524.
20. T. Lee, P. T. Dirlam, J. T. Njardarson, R. S. Glass, and J. Pyun, “Polymerizations With Elemental Sulfur: From Petroleum Refining to Polymeric Materials,” *Journal of the American Chemical Society* 144 (2022): 5–22.
21. Y. Zhang, R. S. Glass, K. Char, and J. Pyun, “Recent Advances in the Polymerization of Elemental Sulphur, Inverse Vulcanization and Methods to Obtain Functional Chalcogenide Hybrid Inorganic/Organic Polymers (CHIPs),” *Polymer Chemistry* 10 (2019): 4078–4105.
22. K. W. Park and E. M. Leitao, “The Link to Polysulfides and Their Applications,” *Chemical Communications* 57 (2021): 3190–3202.

23. R. Hu, X. Yang, A. Qin, and B. Z. Tang, "AIE Polymers in Sensing, Imaging and Theranostic Applications," *Materials Chemistry Frontiers* 5 (2021): 4073–4088.
24. J. J. Griebel, G. Li, R. S. Glass, K. Char, and J. Pyun, "Kilogram Scale Inverse Vulcanization of Elemental Sulfur to Prepare High Capacity Polymer Electrodes for Li-S Batteries," *Journal of Polymer Science* 53 (2015): 173.
25. I. Gomez, O. Leonet, J. A. Blazquez, and D. Mecerreyes, "Inverse Vulcanization of Sulfur Using Natural Dienes as Sustainable Materials for Lithium–Sulfur Batteries," *ChemSusChem* 9 (2016): 3419–3425.
26. A. Hoefling, Y. J. Lee, and P. Theato, "Sulfur-Based Polymer Composites From Vegetable Oils and Elemental Sulfur: A Sustainable Active Material for Li–S Batteries," *Macromolecular Chemistry and Physics* 218 (2017): 1600303.
27. T. S. Kleine, R. S. Glass, D. L. Lichtenberger, et al., "100th Anniversary of Macromolecular Science Viewpoint: High Refractive Index Polymers From Elemental Sulfur for Infrared Thermal Imaging and Optics," *ACS Macro Letters* 9 (2020): 245–259.
28. J. J. Griebel, S. Namnabat, E. T. Kim, et al., "New Infrared Transmitting Material via Inverse Vulcanization of Elemental Sulfur to Prepare High Refractive Index Polymers," *Advanced Materials* 26 (2014): 3014–3018.
29. J. J. Griebel, N. A. Nguyen, S. Namnabat, et al., "Dynamic Covalent Polymers via Inverse Vulcanization of Elemental Sulfur for Healable Infrared Optical Materials," *ACS Macro Letters* 4 (2015): 862.
30. S. J. Tonkin, L. N. Pham, J. R. Gascooke, et al., "Thermal Imaging and Clandestine Surveillance Using Low-Cost Polymers With Long-Wave Infrared Transparency," *Advanced Optical Materials* 11 (2023): 2300058.
31. D. J. Parker, H. A. Jones, S. Petcher, et al., "Low Cost and Renewable Sulfur-Polymers by Inverse Vulcanisation, and Their Potential for Mercury Capture," *Journal of Materials Chemistry A* 5 (2017): 11682–11692.
32. M. P. Crockett, A. M. Evans, M. J. H. Worthington, et al., "Sulfur-Limonene Polysulfide: A Material Synthesized Entirely From Industrial By-Products and Its Use in Removing Toxic Metals From Water and Soil," *Angewandte Chemie International Edition* 55 (2016): 1714–1718.
33. M. J. H. Worthington, R. L. Kucera, I. S. Albuquerque, et al., "Laying Waste to Mercury: Inexpensive Sorbents Made From Sulfur and Recycled Cooking Oils," *Chemistry - A European Journal* 23 (2017): 16219–16230.
34. N. A. Lundquist, M. J. H. Worthington, N. Adamson, et al., "Polysulfides Made From Re-Purposed Waste are Sustainable Materials for Removing Iron From Water," *RSC Advances* 8 (2017): 1232.
35. L. A. Limjuco, G. M. Nisola, K. J. Parohinog, et al., "Water-Insoluble Hydrophilic Polysulfides as Microfibrous Composites Towards Highly Effective and Practical Hg<sup>2+</sup> Capture," *Chemical Engineering Journal* 378 (2019): 122216.
36. A. D. Tikoalu, N. A. Lundquist, and J. M. Chalker, "Mercury Sorbents Made by Inverse Vulcanization of Sustainable Triglycerides: The Plant Oil Structure Influences the Rate of Mercury Removal From Water," *Advanced Sustainable Systems* 4 (2020): 1.
37. Y. Liao, M. Liu, J. Liu, et al., "Cu-Nanoparticle-Decorated Sulfur-Based Polymers for Highly Sensitive Nonenzymatic Glucose Detection," *New Journal of Chemistry* 45 (2021): 16205–16212.
38. A. G. Simmonds, J. J. Griebel, J. Park, et al., "Inverse Vulcanization of Elemental Sulfur to Prepare Polymeric Electrode Materials for Li–S Batteries," *ACS Macro Letters* 3 (2014): 229–232.
39. P. Joia, F. V. Paulovich, D. Coimbra, J. A. Cuminato, and L. G. Nonato, "Local Affine Multidimensional Projection," *IEEE Transactions on Visualization and Computer Graphics* 17 (2011): 2563–2571.
40. M. P. Neto, A. C. Soares, O. N. Oliveira, and F. V. Paulovich, "Machine Learning Used to Create a Multidimensional Calibration Space for Sensing and Biosensing Data," *Bulletin of the Chemical Society of Japan* 94 (2021): 1553–1562.
41. P.-N. Tan, M. Steinbach, and V. Kumar, *Introduction to Data Mining*, 1st ed. (Pearson, 2005).
42. G. James, D. Witten, T. Hastie, and R. Tibshirani, *An Introduction to Statistical Learning, Springer Texts in Statistics*, vol. 103 (Springer, 2013).
43. L. Breiman, J. Friedman, R. Olshen, and C. Stone, *Classification and Regression Trees* (Chapman and Hall/CRC, 1984).
44. M. P. Neto and F. V. Paulovich, "Explainable Matrix - Visualization for Global and Local Interpretability of Random Forest Classification Ensembles," *IEEE Transactions on Visualization and Computer Graphics* 27 (2021): 1427–1437.
45. S. Varma and R. Simon, "Bias in Error Estimation When Using Cross-Validation for Model Selection," *BMC Bioinformatics* 7 (2006): 91.
46. I. Tsamardinos, A. Rakhshani, and V. Lagani, *Artificial Intelligence: Methods and Applications* (Springer International Publishing, 2014), 1.
47. R. Kohavi, "A Study of Cross-Validation and Bootstrap for Accuracy Estimation and Model Selection," 1995.
48. C. N. R. Rao, R. Venkataraghavan, and T. R. Kasturi, "Contribution to the Infrared Spectra of ORGANOSULPHUR Compounds," *Canadian Journal of Chemistry* 42 (1964): 36–42.
49. B. Meyer, "Elemental Sulfur," *Chemical Reviews* 76 (1976): 367–388.
50. X. Guo, J. Huang, Y. Wei, Q. Zeng, and L. Wang, "Fast and Selective Detection of Mercury Ions in Environmental Water by Paper-Based Fluorescent Sensor Using Boronic Acid Functionalized MoS<sub>2</sub> Quantum Dots," *Journal of Hazardous Materials* 381 (2020): 120969.
51. H. T. Ratte, "Bioaccumulation and Toxicity of Silver Compounds: A Review," *Environmental Toxicology and Chemistry* 18 (1999): 89–108.
52. Y. Zhou, L. Tang, X. Xie, et al., "Sensitive Impedimetric Biosensor Based on Duplex-Like DNA Scaffolds and Ordered Mesoporous Carbon Nitride for Silver(I) Ion Detection," *Analyst* 139 (2014): 6529.
53. T.-L. HO, "Hard Soft Acids Bases (HSAB) Principle and Organic Chemistry," *Chemical Reviews* 75 (1975): 1–20.
54. J. Dai, L. Yao, X. Gao, et al., "To Achieve Ultrasensitive Electrochemical Detection of Mercury Ions Employing Metallic 1T-MoS<sub>2</sub> Nanosheets," *Electrochimica Acta* 355 (2020): 136800.
55. S. Katiyar, W. Hou, J. L. Rodriguez, et al., "Building a High-Potential Silver–Sulfur Redox Reaction Based on the Hard–Soft Acid–Base Theory," *Energy & Fuels* 38 (2024): 11233–11239.
56. L. N. Furini, E. Feitosa, P. Alessio, M. H. Shimabukuro, A. Riul, and C. J. L. Constantino, "Tuning the Nanostructure of DODAB/Nickel Tetrasulfonated Phthalocyanine Bilayers in LbL Films," *Materials Science and Engineering: C* 33 (2013): 2937–2946.
57. Z. Wu, L. Xie, Y. Xiao, and D. Wang, "Silver Wrapped MoS<sub>2</sub> Hybrid Electrode Materials for High-Performance Supercapacitor," *Journal of Alloys and Compounds* 708 (2017): 763–768.
58. R. Minghim, F. V. Paulovich, and A. d. A. Lopes, "Proceedings of SPIE 6060," 2006.
59. F. V. Paulovich, M. L. Moraes, R. M. Maki, M. Ferreira, O. N. Oliveira, Jr., and M. C. F. de Oliveira, "Information Visualization Techniques for Sensing and Biosensing," *Analyst* 136 (2011): 1344.
60. I. A. and B. Dimsdale, "Proceedings of the First IEEE Conference on Visualization: Visualization 90," 1990.
61. J. C. Soares, F. M. Shimizu, A. C. Soares, L. Caseli, J. Ferreira, and O. N. Oliveira, Jr., "Supramolecular Control in Nanostructured Film Architectures for Detecting Breast Cancer," *Applied Materials and Interfaces* 7 (2017): 11833.

62. WHO, "Silver in Drinking-Water," 2003.
63. D. M. dos Santos, R. M. Cardoso, F. L. Migliorini, et al., "Advances in 3D Printed Sensors for Food Analysis," *TrAC, Trends in Analytical Chemistry* 154 (2022): 116672.
64. Z. Q. Zhao, X. Chen, Q. Yang, J. H. Liu, and X. J. Huang, "Selective Adsorption Toward Toxic Metal Ions Results in Selective Response: Electrochemical Studies on a Polypyrrole/Reduced Graphene Oxide Nanocomposite," *Chemical Communications* 48 (2012): 2180–2182.
65. P. Yan, W. Zhao, F. McBride, et al., "Mechanochemical Synthesis of Inverse Vulcanized Polymers," *Nature Communications* 13 (2022): 4824.
66. Y. Lyu and Q. Su, "The Exploration of the Inverse Vulcanization Mechanism of Tung Oil by Controlling the Oxygen and Moisture Presence During Reactions," *Polymers and Polymer Composites* 31 (2023): 81255.
67. I. Gomez, D. Mecerreyes, J. A. Blazquez, et al., "Inverse Vulcanization of Sulfur With Divinylbenzene: Stable and Easy Processable Cathode Material for Lithium-Sulfur Batteries," *Journal of Power Sources* 329 (2016): 72–78.
68. S. Fleutot, J. C. Dupin, G. Renaudin, and H. Martinez, "Intercalation and Grafting of Benzene Derivatives Into Zinc–Aluminum and Copper–Chromium Layered Double Hydroxide Hosts: An XPS Monitoring Study," *Physical Chemistry Chemical Physics* 13 (2011): 17564–17578.
69. S. Z. Zeng, Y. Yao, X. Zeng, et al., "A Composite of Hollow Carbon Nanospheres and Sulfur-Rich Polymers for Lithium-Sulfur Batteries," *Journal of Power Sources* 357 (2017): 11–18.
70. D. Wang, Z. Tang, S. Fang, et al., "The Use of Inverse Vulcanised Polysulfide as an Intelligent Interfacial Modifier in Rubber/Carbon Black Composites," *Carbon N. Y* 184 (2021): 409–417.
71. J. Wang, B. Deng, H. Chen, X. Wang, and J. Zheng, "Removal of Aqueous hg(II) by Polyaniline: Sorption Characteristics and Mechanisms," *Environmental Science & Technology* 43 (2009): 5223–5228.
72. Y. Sun, C. Yang, Y. Fu, T. Guo, G. Yan, and J. Hu, "Sulfur-Containing Adsorbent Made by Inverse Vulcanization of Sulfur/Oleylamine/Potato Starch for Efficient Removal of hg(II) Ions," *Journal of Environmental Chemical Engineering* 11 (2023): 109806.
73. X. Guo, M. Li, A. Liu, M. Jiang, X. Niu, and X. Liu, "Adsorption Mechanisms and Characteristics of Hg<sup>2+</sup> Removal by Different Fractions of Biochar," *Water (Basel)* 12 (2020): 82105.
74. A. C. Soares, J. C. Soares, D. M. dos Santos, et al., "Nanoarchitectonic E-Tongue of Electrospun Zein/Curcumin Carbon Dots for Detecting *Staphylococcus Aureus* in Milk," *Omega* 8 (2023): 13721–13732.
75. L. Caseli, J. Gruber, R. W. C. Li, and L. O. Péres, "Investigation of the Conformational Changes of a Conducting Polymer in Gas Sensor Active Layers by Means of Polarization-Modulation Infrared Reflection Absorption Spectroscopy (PM-IRRAS)," *Langmuir* 29 (2013): 2640–2645.
76. C. Feng, P. Zhao, L. Wang, et al., "Fluorescent Electronic Tongue Based on Soluble Conjugated Polymeric Nanoparticles for the Discrimination of Heavy Metal Ions in Aqueous Solution," *Polymer Chemistry* 10 (2019): 2256–2262.
77. H. Kiani, B. Beheshti, A. M. Borghei, and M. H. Rahmati, "Application of a Voltammetric Electronic Tongue Combined With Chemometric Approaches for the Early Classification of Heavy Metals in Sunflower Oil," *Journal of Food Processing and Preservation* 45 (2021): 1.
78. H. Spelthahn, D. Kirsanov, A. Legin, et al., "Development of a Thin-Film Sensor Array for Analytical Monitoring of Heavy Metals in Aqueous Solutions," *Physica Status Solidi. Applications and Materials Science* 209 (2012): 885.
79. T. Lu, A. Al-Hamry, J. Hao, Y. Liu, Y. Qu, and O. Kanoun, "Machine Learning-Based Multi-Level Fusion Framework for a Hybrid Voltammetric and Impedimetric Metal Ions Electronic Tongue," *Chem* 10 (2022): 474.
80. K. B. R. Teodoro, F. M. Shimizu, V. P. Scagion, and D. S. Correa, "Sensors Actuators," *B Chem* 290 (2019): 387.
81. K. T. Paula, S. N. C. Santos, M. H. M. Facure, et al., "Fabrication of Interdigitated Electrodes of Graphene Oxide/Silica by Femtosecond Laser-Induced Forward Transfer for Sensing Applications," *Journal of Applied Physics* 133 (2023): 089902.
82. J. E. Oliveira, V. Grassi, V. P. Scagion, L. H. C. Mattoso, G. M. Glenn, and E. S. Medeiros, "Sensor Array for Water Analysis Based on Interdigitated Electrodes Modified With Fiber Films of Poly(Lactic Acid)/Multiwalled Carbon Nanotubes," *IEEE Sensors Journal* 13 (2013): 759.

## Supporting Information

Additional supporting information can be found online in the Supporting Information section.